Adjustable Fragmentation in Laser Desorption/Ionization from Laser-Induced Silicon Microcolumn Arrays

Yong Chen and Akos Vertes*

Department of Chemistry, Institute for Proteomics Technology and Applications, The George Washington University, Washington, DC 20052

Laser-induced silicon microcolumn arrays (LISMA) were developed as matrix-free substrates for soft laser desorption/ionization mass spectrometry (SLDI-MS). When low-resistivity silicon wafers were irradiated in air, sulfur hexafluoride, or water environment with multiple pulses from a $3\times\omega$ mode-locked Nd:YAG laser, columnar structures were formed on the surface. The radii of curvature of the column tips varied with the processing environment, ranging from ∼120 nm in water, to <1 μm in SF$_6$, and to ∼2 μm in air. In turn, these microcolumn arrays were used as matrix-free soft laser desorption substrates. In SLDI-MS experiments with a nitrogen laser, the microcolumn arrays obtained in water environment readily produced molecular ions for peptides and synthetic polymers at low laser fluence. These surfaces demonstrated the best ion yield among the three arrays. The threshold laser fluence and ion yield were comparable to those observed in matrix-assisted laser desorption/ionization. Low-femtomole sensitivity and ∼6000 Da mass range were achieved. At elevated laser fluence, efficient in-source decay was observed and extensive peptide sequence information was extracted from the resulting mass spectra. The versatility of LISMA was attributed to confinement effects due to the submicrometer morphology and to the surface, thermal, and optical properties of processed silicon.

The discovery of matrix-assisted laser desorption/ionization (MALDI) as a soft ionization technique in the late 1980s greatly expanded the applications of mass spectrometry (MS) in the analysis of thermally labile large biomolecules and synthetic polymers.[1,2] In this method, proxy substances, called matrixes, were used to efficiently absorb laser energy and promote the ion formation of the large molecules otherwise prone to thermal degradation. Matrixes initially came in two forms. Tanaka and co-workers used cobalt nanoparticles to absorb the laser energy and glycerol solution to provide the protons,[1] whereas Karas and Hillenkamp used small organic molecules that strongly absorbed

the energy at a specific laser wavelength.[2] The organic matrixes typically have a high ionization cross section and provide protons for the soft ionization of analytes. The latter approach is extensively used in the high-mass range (600 < m/z < 200 000), due to its high ionization efficiency and the simplicity of sample preparation.

In the low-mass region (m/z < 600), the utility of MALDI is limited due to spectral interference from matrix-related ions. The spectrum in the m/z < 600 region is dominated by the fragments, molecular ions, clusters, and matrix adducts that obscure the signal for small molecules of interest, such as drug metabolites and small peptides. The high abundance of matrix-related ions in the laser plume also causes strong space-charge effects in the ion source and deteriorates the ion optical performance.[3] The excessive amount of matrix ions saturates the detector, resulting in compromised sensitivity for the analyte signal. Moreover, even at threshold laser fluence, the high density of matrix molecules in the plume may result in signal suppression for low-abundance analytes.[4,5]

In an attempt to minimize the matrix interference, the method of surface-assisted laser desorption/ionization was introduced. In its initial form, micrometer-sized graphite particles were used as the laser absorbing substrate and glycerol as the protonating agent.[6,7] In an alternative approach, 2,5-dihydroxybenzoic acid (DHB)-infused silica sol−gel served as an efficient soft laser desorption/ionization (SLDI) surface.[8] It was found, however, that at elevated laser power the DHB signal appeared in the spectrum.[8] Promising SLDI performance was demonstrated in other sol−gel-based methods, in which acidic buffer solutions were used for protonation.[9,10] Polymer substrates also appeared capable of SLDI for small molecules.[11,12] Several groups found carbon nanotubes to work as SLDI substrate.[13,14] In these experiments,

* To whom correspondence should be addressed. E-mail: vertes@gwu.edu. Phone: (202) 994-2717. Fax: (202) 994-5873.

(1) Tanaka, K.; Waki, H.; Ido, Y.; Akita, S.; Yoshida, Y.; Yoshida, T. *Rapid Commun. Mass Spectrom.* **1988**, *2*, 151−153.

(2) Karas, M.; Hillenkamp, F. *Anal. Chem.* **1988**, *60*, 2299−2301.

(3) Weickhardt, C.; Moritz, F.; Grotemeyer, J. *Mass Spectrom. Rev.* **1996**, *15*, 139−162.

(4) Knochenmuss, R.; Stortelder, A.; Breuker, K.; Zenobi, R. *J. Mass Spectrom.* **2000**, *35*, 1237−1245.

(5) Knochenmuss, R. *Anal. Chem.* **2003**, *75*, 2199−2207.

(6) Sunner, J.; Dratz, E.; Chem, Y. *Anal. Chem.* **1995**, *67*, 4335−4342.

(7) Dale, M. J. K.; Knochenmuss, R.; Zenobi, R. *Anal. Chem.* **1996**, *68*, 3321−3329.

(8) Lin, Y.-S.; Chen, Y.-C. *Anal. Chem.* **2002**, *74*, 5793−5798.

(9) Hoang, T. T.; Chen, Y.; May, S. W.; Browner, R. F. *Anal. Chem.* **2004**, *76*, 2062−2070.

(10) Chen, C.-T.; Chen, Y.-C. *Rapid Commun. Mass Spectrom.* **2004**, *18*, 1956−1964.

(11) Peterson, D. S.; Luo, Q.; Hilder, E. F.; Svec, F.; Frechet, J. M. J. *Rapid Commun. Mass Spectrom.* **2004**, *18*, 1504−1512.

alkali adducts were the main ionic products from neat nanotubes,[13] whereas acid-treated nanotubes produced predominantly protonated ions.[14]

For its purity and amenability to surface modifications, e.g., photolithography, photoelectrochemical etching, and silylation, microelectronics grade silicon is an ideal choice for high-sensitivity SLDI-MS. In 1999, Siuzdak and co-workers developed the desorption/ionization on silicon (DIOS) method that used nanoporous silicon from galvanostatic etching as a SLDI substrate.[15] Initial research on DIOS indicated that silicon pore size and overall porosity, surface hydrophobicity, and storage time in the ambient environment had an important impact on the SLDI performance.[16−22] Hydrophobic silylation gave DIOS surfaces extended stability and ultrahigh MS sensitivity.[23]

There are alternative methods to produce nanostructured silicon layers. Void-column networks of nanocrystalline silicon, produced by high-density plasma deposition, were reported to possess high porosity and unique properties similar to electrochemically etched porous silicon.[24] Cuiffi and co-workers demonstrated that this thin film could also be utilized in SLDI mass analysis for molecules of up to 6000 Da.[25] Silylated single-crystal silicon nanowires, synthesized with a gold nanoparticle-catalyzed, vapor−liquid−solid technique, were found to be a promising substrate for direct biomolecule analysis at extremely low laser fluences.[26] With nanoparticles as a mask, Finkel et al. used reactive ion etching to generate ordered silicon nanocavity arrays that served as an SLDI surface.[27] Recently, Okuno and co-workers demonstrated that surfaces possessing submicrometer structure, such as porous alumina or polyethylene coated with metals, lithographically fabricated submicrometer silicon groove arrays, and even silicon wafer roughened with sandpaper, could act as SLDI substrates.[28]

One of the common features in these diverse matrixless SLDI methods is the use of micro- or nanostructured surfaces as a substrate. Alimpiev et al. conducted mechanistic studies on SLDI from etched carbon and silicon surfaces and concluded that three conditions had to be fulfilled for efficient ion production: sufficient absorption of the laser energy, micro- or nanostructured substrate surface, and a $pK_a > \sim4$ for the adsorbate.[29] The first two conditions prescribe the requirements for the properties of the SLDI surfaces. The majority of the explored surfaces by far are nanoporous structures. The limitation of the structures tested thus far includes limited stability under ambient conditions and the lack of control over structure-specific fragmentation.

Our goal in this study was to develop alternative surface structure with nanoscopic features that were sufficiently robust for SLDI applications. It was shown that repeated exposure of a polished silicon surface to nanossecond[30,31] and femtosecond[32] laser pulses could produce two-dimensional arrays of conical protrusions on silicon surface. These structures are called laser-induced microcolumn arrays (LISMA) hereon. The periodicity, thickness, height, and radius of tip curvature for these microcolumns varied with the environment in which the target was irradiated[31−35] and with the laser pulse length, applied fluence, and number of laser pulses.[36−39] In a remarkable departure from unstructured silicon that is transparent to below-band gap radiation ($\lambda > 1.1\ \mu m$), the microcolumn arrays demonstrate close-to-unity absorptance from near UV (> 250 nm) to near-IR (<2.5 μm).[38,39] The new surface morphology and optoelectronic properties of these microstructured surfaces are being explored for field emission, infrared photodetector, sensor, and display applications. These same unique properties also make the laser-induced silicon microcolumn arrays a promising candidate for SLDI-MS.

Silicon-based lab-on-a-chip techniques enabled the rapid and automated separation and identification of proteins.[40−42] As the laser irradiation process we use to produce the silicon microcolumn arrays does not involve lengthy chemical etching with corrosive reagents, these surfaces can be easily integrated into

(12) Woldegiorgis, A.; von Kieseritzky, F.; Dahlstedt, E.; Hellberg, J.; Brinck, T.; Roeraade, J. *Rapid Commun. Mass Spectrom.* **2004**, *18*, 841−852.

(13) Xu, S.; Li, Y.; Zou, H.; Qiu, J.; Guo, Z.; Guo, B. *Anal. Chem.* **2003**, *75*, 6191−6195.

(14) Chen, W.-Y.; Wang, L.-S.; Chiu, H.-T.; Chen, Y.-C.; Lee, C.-Y. *J. Am. Soc. Mass Spectrom.* **2004**, *15*, 1629−1635.

(15) Wei, J.; Buriak, J. M.; Siuzdak, G. *Nature* **1999**, *399*, 243−246.

(16) Shen, Z.; Thomas, J. J.; Averbuj, C.; Broo, K. M.; Engelhard, M.; Crowell, J. E.; Finn, M. G.; Siuzdak, G. *Anal. Chem.* **2001**, *73*, 612−619.

(17) Thomas, J. J.; Shen, Z.; Crowell, J. E.; Finn, M. G.; Siuzdak, G. *Proc. Natl. Acad. Sci. U.S.A.* **2001**, *98*, 4932−4937.

(18) , Kruse, R. A.; Li, X.; Bohn, P. W.; Sweedler, J. V. *Anal. Chem.* **2001**, *73*, 3639−3645.

(19) Kruse, R. A.; Rubakhin, S. S.; Romanova, E. V.; Bohn, P. W.; Sweedler, J. V. *J. Mass Spectrom.* **2001**, *36*, 1317−1322.

(20) Zhang, Q.; Zou, H.; Guo, Z.; Zhang, Q.; Chen, X.; Ni, J. *Rapid Commun. Mass Spectrom.* **2001**, *15*, 217−223.

(21) Lewis, W. G.; Shen, Z.; Finn, M. G.; Siuzdak, G. *Int. J. Mass Spectrom.* **2003**, *226*, 107−116.

(22) Go, E. P.; Shen, Z.; Harris, K.; Siuzdak, G. *Anal. Chem.* **2003**, *75*, 5475−5479.

(23) Trauger, S. A.; Go, E. P.; Shen, Z.; Apon, J. V.; Compton, B. J.; Bouvier, E. S. P.; Finn, M. G.; Siuzdak, G. *Anal. Chem.* **2004**, *76*, 4484−4489.

(24) Kalkan, A. K.; Bae, S.; Li, H.; Hayes, D. J.; Fonash, S. J. *J. Appl. Phys.* **2000**, *88*, 555−561.

(25) Cuiffi, J. D.; Hayes, D. J.; Fonash, S. J.; Brown, K. N.; Jones, A. D. *Anal. Chem.* **2001**, *73*, 1292−1295.

(26) Go, E. P.; Apon, J. V.; Luo, G.; Saghatelian, A.; Daniels, R. H.; Sahi, V.; Dubrow, R.; Cravatt, B. F.; Vertes, A.; Siuzdak, G. *Anal. Chem.* **2005**, *77*, 1641−1646.

(27) Finkel, N. H.; Prevo, B. G.; Velev, O. D.; He, L. *Anal. Chem.* **2005**, *77*, 1088−1095.

(28) Okuno, S.; Arakawa, R.; Okamoto, K.; Matsui, Y.; Seki, S.; Kozawa, T.; Tagawa, S.; Wada, Y. *Anal. Chem.* **2005**, *77*, 5364−5369.

(29) Alimpiev, S.; Nikiforov, S.; Karavanskii, V.; Minton, T.; Sunner, J. *J. Chem. Phys.* **2001**, *115*, 1891−1901.

(30) Rothenberg, J. E.; Kelly, R. *Nucl. Instrum. Methods Phys. Res.* **1984**, *B1*, 291−300.

(31) Pedraza, A. J.; Fowlkes, J. D.; Lowndes, D. H. *Appl. Phys. Lett.* **1999**, *74*, 2322−2324.

(32) Her, T.-H.; Finlay, R. J.; Wu, C.; Deliwala, S.; Mazur, E. *Appl. Phys. Lett.* **1998**, *73*, 1673−1675.

(33) Pedraza, A. J.; Fowlkes, J. D.; Lowndes, D. H. *Appl. Phys. Lett.* **2000**, *77*, 3018−3020.

(34) Fowlkes, J. D.; Pedraza, A. J.; Lowndes, D. H. *Appl. Phys. Lett.* **2000**, *77*, 1629−1631.

(35) Shen, M. Y.; Crouch, C. H.; Carey, J. E.; Mazur, E. *Appl. Phys. Lett.* **2004**, *85*, 5694−5696.

(36) Her, T.-H.; Finlay, R. J.; Wu, C.; Mazur, E. *Appl. Phys. A* **2000**, *70*, 383−385.

(37) Pedraza, A. J.; Fowlkes, J. D.; Guan, Y.-F. *Appl. Phys. A* **2003**, *77*, 277−284.

(38) Crouch, C. H.; Carey, J. E.; Warrender, J. M.; Aziz, M. J.; Mazur, E.; Genin, F. Y. *Appl. Phys. Lett.* **2004**, *84*, 1850−1852.

(39) Wu, C.; Crouch, C. H.; Zhao, L.; Carey, J. E.; Younkin, R.; Levinson, J. A.; Mazur, E.; Farrell, R. M.; Gothoskar, P.; Karger, A. *Appl. Phys. Lett.* **2001**, *78*, 1850−1852.

(40) Ekstrom, S.; Onnerfjord, P.; Nilsson, J.; Bengtsson, M.; Laurell, T.; Marko-Varga, G. *Anal. Chem.* **2000**, *72*, 286−293.

(41) Ekstrom, S.; Ericsson, D.; Onnerfjord, P.; Bengtsson, M.; Nilsson, J.; Marko-Varga, G.; Laurell, T. *Anal. Chem.* **2001**, *73*, 214−219.

(42) Brivio, M.; Fokkens, R. H.; Verboom, W.; Reinhoudt, D. N.; Tas, N. R.; Goedbloed, M.; van den Berg, A. *Anal. Chem.* **2002**, *74*, 3972−3976.

microfluidics-based analytical systems for integrated SLDI-MS. In principle, used microcolumn surfaces can also be regenerated by additional processing with laser radiation.

In this article, we demonstrate that picosecond laser irradiation can also be used to produce microcolumn arrays on silicon and that the resulting structures are efficient SLDI substrates for small-molecule mass spectrometry. The array properties, such as periodicity, column thickness and height, and radius of tip curvature, were changed by varying the environment and the parameters in laser processing. This also enabled us to explore the dependence of SLDI yields on the surface morphology. Furthermore, the utility of silicon microcolumn arrays in inducing structure-specific fragmentation at elevated laser fluence was studied.

EXPERIMENTAL SECTION

Materials. Single-side polished mechanical grade, low-resistivity ($\sim$0.001–0.005 $\Omega \cdot$cm) p-type silicon wafers (Si:B $\langle 100 \rangle$, 280$\pm$20 μm in thickness) were purchased from University Wafer (South Boston, MA). Ambient air, deionized water (18.2 M$\Omega \cdot$cm), and sulfur hexafluoride gas (Spectra Gases, Inc., Branchburg, NJ) were used as background media during laser microstructuring. A peptide and protein MALDI-MS calibration kit (MSCAL1), HPLC grade substance P, angiotensin I, bovine insulin, ethanol, methanol, and reagent grade DHB and α-cyano-4-hydroxycinnamic acid (CHCA) were obtained from Sigma Chemical Co. (St. Louis, MO). Reagent grade trifluoroacetic acid (TFA) was obtained from Aldrich (Milwaukee, WI). Acetonitrile solvent (HPLC grade) was purchased from Fisher Scientific (Springfield, NJ). Poly(propylene glycol) (PPG1000, average molecular weight 1000) and PEG400 (average molecular weight 400) were obtained from American Polymer Standards Corp. (Mentor, OH) and Sigma Chemical Co., respectively.

Preparation of Silicon Microcolumn Arrays. Silicon wafers were cleaved into desired sizes, cleaned sequentially with methanol, ethanol, and deionized water, air-dried, and then exposed to repeated laser irradiations in the presence of air, SF$_6$ gas, or deionized water. For microstructuring in air or water, double-sided tape was used to fix the cleaned silicon wafer to the bottom of a Petri dish filled with ambient air or deionized water, respectively. For processing in SF$_6$ gas, a small vacuum chamber was assembled with a quartz window and a blank flange on two opposing arms of a four-way cross. The silicon wafer was attached to the inside wall of the blank flange. The chamber was pumped down to a base pressure of 0.01 Torr and backfilled with SF$_6$ gas to various pressures. A mode-locked frequency-tripled Nd:YAG laser with 355-nm wavelength and 22-ps pulse length (PL2143, EKSPLA, Vilnius, Lithuania) was operated at 2 Hz as the laser source for surface microstructuring. A UV grade fused-silica lens (25.4-cm effective focal length, Thorlabs, Newton, NJ) focused the laser beam through the quartz window onto the silicon target from a distance of $\sim$20 cm, resulting in a $\sim$1-mm-diameter focal spot. Scanning electron microscopes (SEM; LEO 1460VP, Carl Zeiss, Thornwood, NY, and FE-SEM S4700, Hitachi, Pleasanton, CA) were used to examine the surface morphology of the laser-processed spot. The SEM images were characterized with the UTHSCSA ImageTool program (V3.0, developed at the University of Texas Health Science Center (San Antonio, TX).

Mass Spectrometry. The ionization threshold fluence measurement was carried out on a home-built linear time-of-flight (TOF) mass spectrometer. The detailed description of the instrument can be found elsewhere.[43] Briefly, ions generated with a nitrogen laser of 337-nm wavelength and 4-ns pulse length (VSL-337ND, Laser Science Inc., Newton, MA) were accelerated to 25 kV, and the ion current was recorded with a 1.5-GHz digital oscilloscope (LC684DXL, LeCroy, Chestnut Ridge, NY). A variable attenuator (935–5-OPT, Newport, Fountain Valley, CA) was used to adjust the laser fluence. Actual laser fluence values were calculated from the laser pulse energy measured with a pyroelectric Joule meter (model J4-05, Molectron, Portland, OR) and the laser focal area determined from the size of the burn mark on a photographic paper.[43]

A curved field reflectron TOF mass spectrometer (Axima CFR, Shimadzu-Kratos, Manchester, UK) was used to collect the spectra at high resolution and sensitivity. In this system, the laser beam from a nitrogen laser was focused to a $\sim$100-μm-diameter area on the target. Laser energy could be tuned in the range of 0–180 expressed in arbitrary units. Assuming that the neutral density filter, standard in these instruments, did not change the focused spot size, this scale also corresponded to proportional settings of laser fluence and laser irradiance (i.e., laser power). All mass spectra shown in this report are the average of 100 laser shots acquired in reflectron mode, using 100-ns-delayed, 2.5-kV extraction and a 20-kV acceleration voltage.

The silicon substrates were attached to the MALDI target plate with conductive double-sided carbon tape. Since the thickness of the silicon and carbon tape altered the electric field and flight length in the mass spectrometer, the system was recalibrated to provide correct mass assignments.

RESULTS AND DISCUSSION

Preparation and Morphology of Silicon Microcolumn Arrays. Surface laser microstructuring was conducted on low-resistivity silicon wafers with the picosecond laser. Preparation conditions, such as the processing environment and laser fluence, were varied to produce microcolumn arrays with the best SLDI performance. Microstructuring in air and water environment was carried out at ambient conditions, whereas processing in SF$_6$ gas was conducted between 1 Torr and 1 atm pressure. Upon repeated laser exposure, the illuminated spot on the silicon wafer turned dark (less reflective) compared to the unexposed area. As the number of laser shots increased, this area finally became black, exhibiting a strong contrast to the unprocessed glossy bulk silicon surface. In Figure 1, SEM images demonstrate the surface morphology of the silicon wafers processed in the different environments.

Figure 1A shows the silicon surface irradiated with $\sim$1000 1 J/cm^2 laser pulses in ambient air. The laser shots caused deformation and structuring of the surface. The resulting ubiquitous protrusions were blunt, and their distribution was irregular. The top view (left panel) shows that between the protrusions there are numerous small holes (diameter 3–4 μm), possibly resulting from the eruption of superheated subsurface silicon. In this phenomenon, known as phase explosion, subsurface vapor bubbles form when the surface layer melts and becomes transparent and

(43) Chen, Y.; Vertes, A. *J. Phys. Chem. A* **2003**, *107*, 9754–9761.
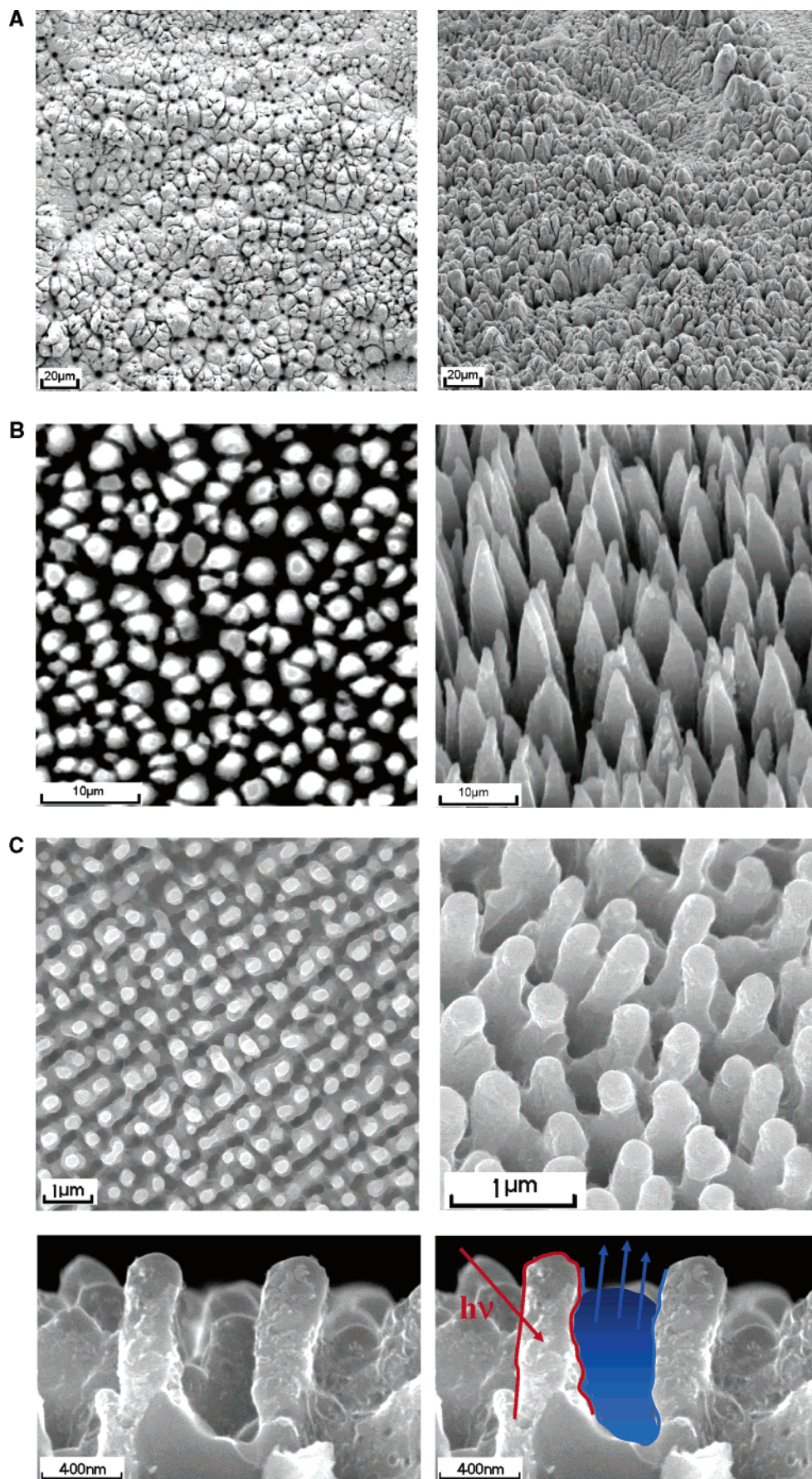
Figure 1. Top (left panels) and side (right panels) views of silicon microcolumn arrays produced (A) in ambient air with 1000 laser shots at 1 J/cm^2, (B) in SF$_6$ gas at 1 atm pressure with 1200 laser shots at 0.4 J/cm^2, and (C) in water with 600 laser shots at 0.13 J/cm^2. Bottom panels show cross sectional view.

explode when they reach a critical size.[44,45] The ensuing vigorous plume expansion at atmospheric pressure results in the rapid cooling and eventual collapse of the plume.[46] In this process, most of the silicon vapor recondenses on the surrounding surface areas and the protrusions are formed.

Applying 1200 laser pulses of 0.4 J/cm^2 fluence in 1 atm SF$_6$ gas environment produced sharp protrusions on the silicon surface, in the form of a quasiperiodic array of microspikes. Figure 1B shows the top (left panel) and the side (right panel) views of the center portion of the array. There are four morphology parameters that characterize the arrays: the periodicity, the diameter and height of the spikes, and the radius of curvature at their tips. The density and size of the microspikes vary corresponding to the laser irradiance distribution across the profile, with thick, tall spikes in the middle, and fine, short ones at the rim. Assuming a TEM$_{00}$ laser beam profile enables us to calculate the local laser fluence, $I(r)$, a particular r distance along the radius.

$$I(r) = \frac{2E}{\pi a^2} e^{-2r^2/a^2}$$

where E is the laser energy and a is the radius where the intensity falls to $1/e^2$ or 13.5% of the intensity in the center. This means that the laser intensity drops by a factor of ~10 going from the center to the perimeter of the focal spot. This change in laser intensity from the center to the rim corresponds to a 3.5−1.5-μm change in the periodicity, 0.75−0.5-μm reduction in the radius of tip curvature, and a 16−5-μm drop in the height of the microspikes.

Arrays of submicrometer microcolumns were generated with 600 laser shots at 0.13 J/cm^2 in water environment, as shown in Figure 1C. The microcolumns average 120 nm in the radius of tip curvature (bottom left panel), 600 nm in average periodicity (top left panel), and 800 nm in height (bottom left panel). The cross sectional view (bottom panels) shows deep troughs between the submicrometer size columns. Unlike in the SF$_6$ gas environment, the size and distribution of the microcolumns produced in water are homogeneous across most of the laser spot. Comparing the side views of the columns for SF$_6$ (right panel in Figure 1B) and water (top right panel in Figure 1C) also indicates conical and cylindrical column morphologies, respectively.

It was proposed that these surface structures were the result of laser-induced silicon vaporization and recondensation.[31−32] The initial laser irradiation causes local surface deformation in the form of capillary waves. Upon further laser exposure, the silicon vapor is preferentially redeposited at the tips of these structures, promoting axial growth and deepening the troughs and canyons. The sharp tips of the resulting microspikes in SF$_6$ gas are attributed to chemical etching by the laser-induced decomposition products from SF$_6$.[32,34,36] The significantly finer structure in water may be attributed to the high thermal conductivity and heat capacity of water, which helps rapidly solidify silicon melt and limits the size of the protrusions.[35]

The black color of laser-processed silicon indicates the close to unit absorptance from the near-UV to near-IR spectrum range.[38,39] This enhanced absorption is due to the defect states in the band gap induced by the structural defects and impurities incorporated during laser ablation.[38,39] The intrinsic absorptance is further increased by the multiple reflections within the array of microcolumns.

Fluence Dependence of Desorption/Ionization. The three types of microstructured silicon substrates were attached to the solid insertion probe of the home-built MALDI-MS using conductive double-sided carbon tape. Stock solutions of substance P (1347.63 Da), angiotensin I (1296.48 Da), and bovine insulin (5733.49 Da) were prepared at ~0.5 nmol/μL concentration in 0.1% TFA solution. A 1.0-μL aliquot of the analyte solutions was directly deposited and air-dried on the silicon substrates.

Protonated substance P signal was successfully detected on silicon microcolumn arrays produced in SF$_6$ and in water (data not shown). LISMA produced in water required ~30 mJ/cm^2 threshold laser fluence for ionization, similar to that required in MALDI experiments under similar conditions.[43] Substrates generated in SF$_6$ gas required 70 mJ/cm^2 laser fluence. Silicon processed in air showed no ability to produce substance P signal. As a control experiment, we also deposited a substance P sample on unmodified silicon surface. No substance P ions were detected in the studied laser fluence range, and only very weak Na$^+$ and K$^+$ ion signal appeared at elevated fluence (90 mJ/cm^2). All studied polypeptides including bovine insulin could be detected on the LISMA produced in water, whereas only small peptides angiotensin I and substance P appeared in the spectra from the substrates produced in SF$_6$ gas.

The correlation between the SLDI performance and the surface morphology can be associated with the variations of several factors, such as the surface area and confinement effects manifesting in, for example, higher optical absorption and lower thermal conductivity. These factors were also considered significant in the DIOS method.[51] For example, the heat conduction is inversely correlated with morphology; i.e., fine microcolumns have lower conductive thermal loss than the bulk material. Furthermore, nanostructured silicon has been reported to have a significantly reduced lattice thermal conductivity due to phonon confinement and boundary scattering.[47,48] Thus, on the microcolumn arrays generated in water, the threshold temperature for desorption/ionization can be reached at lower laser fluence than on the coarser structures.

Another important factor is the near-field effect in the vicinity of the microcolumns.[49] The silicon microcolumns act like antennas and locally enhance the radiation field of the laser, thus reducing the fluence threshold.

Ionization yields can be affected by the presence of electrons in the laser plume due to photoelectric effects. Although the work function of pure ⟨111⟩ silicon surface is 4.83 eV, the microcolumn

(44) Yoo, J. H.; Jeong, S. H.; Mao, X. L.; Greif, R.; Russo, R. E. *Appl. Phys. Lett.* **2000**, *76*, 783−785.

(45) Yoo, J. H.; Borisov, O. V.; Mao, X. L.; Russo, R. E. *Anal. Chem.* **2001**, *73*, 2288−2293.

(46) Vertes, A. In *Laser Ablation: Mechanisms and Applications II*; Miller, J. C., Geohegan, D. B., Eds.; AIP Press: New York, 1994; pp 275−284.

(47) Zou, J.; Balandin, A. *J. Appl. Phys.* **2001**, *89*, 2932−2938.

(48) Qi, J.; White, J. M.; Belcher, A. M.; Masumoto, Y. *Chem. Phys. Lett.* **2003**, *372*, 763−766.

(49) Holz, L.; Semjonow, A.; Lenz, K.; Lau, A.; Richter, W.; Wilhelm, H. *J. Appl. Phys.* **1992**, *72*, 2472−2477.

(50) Frankevich, V.; Knochenmuss, R.; Zenobi, R. *Int. J. Mass Spectrom.* **2002**, *220*, 11−19.

(51) Luo, G.; Chen, Y.; Siuzdak, G.; Vertes, A. *J. Phys. Chem. A* **2005**, *109*, 24450−24456.
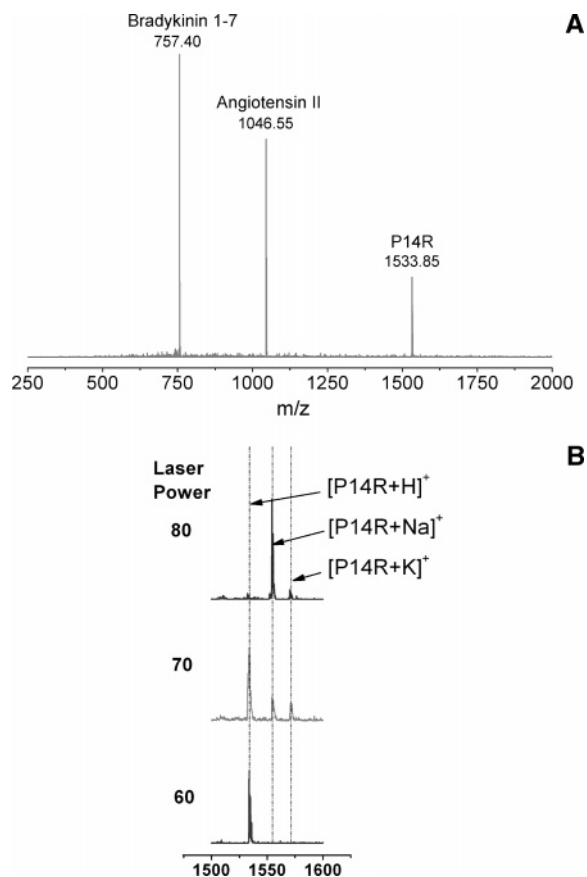
Figure 2. (A) Reflectron mass spectrum of bradykinin fragment 1−7, angiotensin II, and P14R mixture, 1 pmol each, at laser power 60. (B) With increase in laser power, P14R alkali (particularly sodium) adducts become dominant in spectrum.

structure and the presence of the analyte on the surface can reduce this value perhaps even below the photon energy of the nitrogen laser (3.7 eV) used in the desorption experiments. Similar effects were observed in MALDI desorption from metal surfaces.[50] In a delayed extraction experiment, during the initial field-free period substantial electron density can develop. Depending on the experimental conditions, the interaction of these electrons with the laser plume can yield more (electron impact ionization) or less (recombination) positive ions.

Residual solvents retained in the cavities of the LISMA surface are the probable sources of protons that help to ionize peptides on the silicon substrate.[15,18,51] Upon laser irradiation, the enhanced electric field and the photoelectron emission can significantly promote charge separation and ion formation from these solvent molecules.[29]

SLDI at Low Fluences. To further characterize the performance of the LISMA surface produced in water, data were collected on a Shimadzu-Kratos Axima CFR TOF mass spectrometer in the reflectron mode. Bradykinin fragment 1−7 (monoisotopic MW = 756.39), angiotensin II (MW = 1045.53), and a synthetic peptide, Pro_{14}−Arg (P14R, MW = 1532.86), from the MSCAL1 MALDI-MS calibration kit were dissolved at 1 pmol/μL concentration in 0.1% TFA. One microliter of this solution was applied on the LISMA substrate. Mass spectra were acquired at laser power 60 with a low-mass cutoff of 300 Da. As shown in Figure 2A, all three peptides are protonated with no sign of alkali adduction or fragmentation. The laser power setting 60 was

slightly above the ionization threshold for LISMA. This was lower than the necessary laser power of 65 and 80 we determined for the MALDI matrixes CHCA and DHB, respectively. As CHCA requires the lowest laser fluence among the commonly used matrixes,[43] this confirms the utility of LISMA as an efficient SLDI method. In MALDI, the labile synthetic peptide, P14R, tends to fragment at each proline residue forming a series of y-type ions.[52] For this reason, P14R is commonly used as a calibration compound for metastable fragmentation in postsource decay (PSD) experiments. Notably, there is no sign of P14R fragmentation in Figure 2A, proving that at low fluences LISMA imparts negligible internal energy to the analyte. A detection limit of 10 fmol was determined based on the analysis of dilute P14R solutions.

With the increase of laser fluence, alkali adducts appeared in the spectra. Figure 2B shows the redistribution of P14R quasi-molecular ions as the laser power increases from 60 to 80. At laser power 60, there were only protonated P14R molecules. With the laser power increased to 70, sodiated and potassiated P14R peaks also appeared. At laser power 80, the sodiated P14R became the dominant species whereas the abundance of the other two ions diminished.

We also demonstrated that LISMA could desorb and ionize synthetic polymers. Figure 3A shows the mass spectrum of 1 μL of 0.1 μg/μL PPG1000 in 0.1% TFA/30% methanol acquired in reflectron mode at a laser power of 135. Even though no sodium salt was added to the sample, exclusively sodiated PPG peaks appeared in the spectrum. The mass difference between neighboring peaks was 58 Da, reflecting the propylene glycol repeat unit. Other than the marginal signal from alkali and other metal ions in the <60 Da low-mass region (shown in the inset of Figure 3A), there were no background peaks in the spectrum. Figure 3B shows similar results obtained from 100 ng of PEG400 at a laser power setting of 125. The major sodiated PEG oligomer peaks are accompanied by the potassiated PEG satellites.

Structure-Specific Fragmentation. To assess the ability of LISMA surfaces to induce structure-specific peptide fragmentation, P14R spectra were recorded as a function of laser fluence. Fragmentation of the P14R started when the laser power exceeded 75 arbitrary units. Figure 4A shows the spectrum acquired from 1 pmol of P14R at a laser power of 85 in the reflectron mode with the PSD ion gate disabled. For comparison, Figure 4B shows the MALDI PSD spectrum of 1 pmol of P14R desorbed from the CHCA matrix at a laser power of 100. Typically for PSD in MALDI, the fragment ions were mostly y-type species and their derivatives due to NH_3 loss; they were only moderately well focused; and their intensity deteriorated with the loss of just a few residues. In contrast, the peptide fragments from the LISMA surface were mostly sodiated N-terminal ions. Losing the arginine residue produced c14 ions, and sequential proline loss resulted in a series of a-type ions. Compared to the parent species, most fragment ions exhibited significant abundance. The isotope distributions in Figure 4C shows that all fragment ions are well focused throughout the mass range. This indicated that the fragment ions formed instantaneously in the acceleration region; i.e., these ions were produced by in-source decay (ISD). At 85 laser power, the most prominent quasi-molecular ion was the sodiated P14R (see

(52) O'Connor, P. B.; Budnik, B. A.; Ivleva, V. B.; Kaur, P.; Moyer, S. C.; Pittman, J. L.; Costello, C. E. *J. Am. Soc. Mass Spectrom.* **2004**, *15*, 128−132.
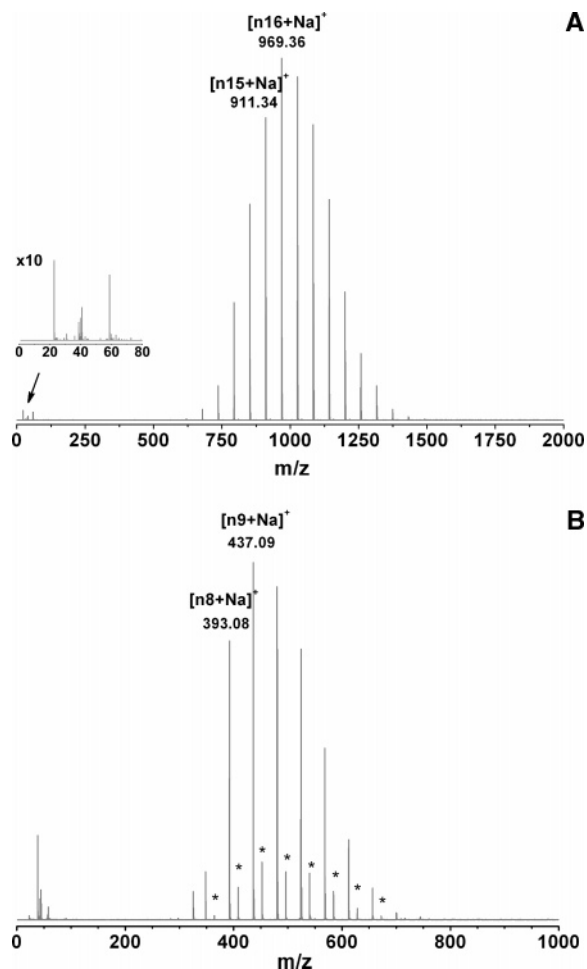
Figure 3. (A) Mass spectrum of 0.1 μg of PPG1000 at laser power 135 with no low-mass cutoff. All PPG peaks are sodiated, and n16 stands for degree of polymerization $n = 16$. Inset indicates a 10× magnified marginal signal from alkali and other metal ions in low-mass region. (B) Mass spectrum of 0.1 μg of PEG400 at power 125. Major peaks are sodiated PEG molecules, whereas asterisks indicate potassium adducts.

panel e in Figure 4C), whereas the protonated P14R peak was marginal.

To demonstrate the ability of LISMA substrates to induce structure-specific fragmentation at elevated laser fluences, 1 pmol of bradykinin was deposited and analyzed at laser power setting of 145 (see Figure 5). Bradykinin exhibited behavior similar to that of P14R in that the low-fluence spectra showed only quasi-molecular ions (Figure 2A), whereas spectra taken at elevated laser fluences showed structure-specific fragmentation (see Figure 5). In addition to c_6 and the a-type ions, y-type fragments were also observed in the bradykinin spectra.

Although in peptide mapping ISD is avoided, in the top-down sequencing approach, it can be very useful in determining the primary structure of peptides. As MALDI is a soft ionization method, the quasi-molecular ions gain only a limited amount of internal energy during ionization. Thus, ISD in MALDI is very inefficient and the peptides undergo metastable fragmentation past the source region (postsource decay) instead.[53] As we demonstrate in Figure 4A, at elevated laser power, LISMA can efficiently

(53) Kocher, T.; Engstrom, A.; Zubarev, R. A. *Anal. Chem.* **2005**, *77*, 172−177.
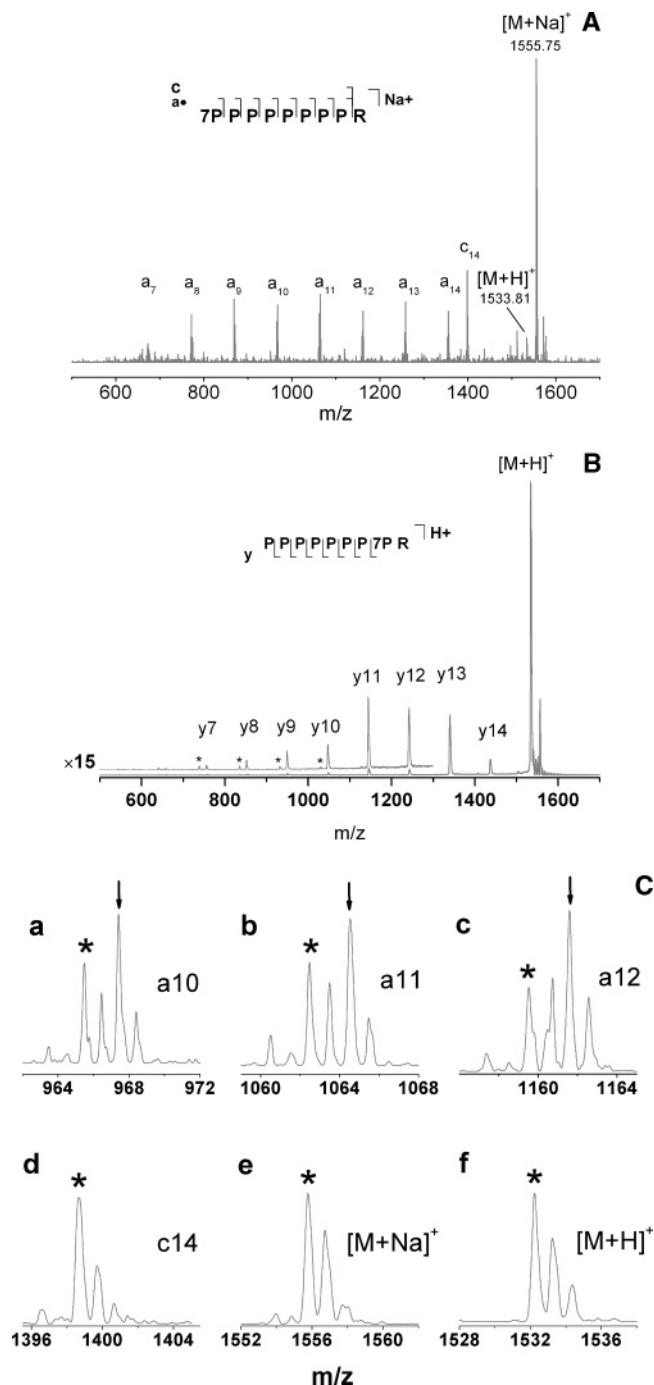
Figure 4. (A) ISD spectrum of 1 pmol of P14R on silicon micro-column array at laser power 85. R and P stand for arginine and proline residues. Sodiated N-terminal fragment ions (a-type and c-type) are observed. (B) PSD spectrum of 1 pmol of P14R in CHCA matrix at laser power 100. Protonated y-type ions are observed. Asterisks mark the y-type ions with ammonia loss. (C) Isotopic profiles of P14R ISD fragment ions: (a) a10, (b) a11, (c) a12, (d) c14, (e) molecular ion $[M + Na]^+$ at laser power 85, and (f) molecular ion $[M + H]^+$ at laser power 60. Asterisks mark the monoisotopic peak in each profile, and neighboring peaks are 1 Da apart.

promote ISD and provide structural information complementary to other peptide sequencing methods. In contrast, at low laser power, LISMA provides molecular weight information for the analysis of intact peptides even as labile as P14R (see Figure 2A). The mechanism behind the versatility of LISMA substrates is unclear, but we believe it can be attributed to the unique properties

$$\overset{y}{\underset{c}{\overset{a}{R|P|P|G|F|S|P|F|R}}}\text{]}^+\text{H}^+$$

Figure 5. ISD spectrum of 1 pmol of bradykinin on silicon microcolumn array at laser power 145.

of the silicon microcolumn structure and possibly to confinement effects. The various factors affecting SLDI from LISMA are discussed below.

(1) Increased Surface Area. Laser structuring of the silicon surface results in an increased surface area. Based in Figure 1C, we can approximate the shape of the microcolumns produced in water by cylinders with a hemispherical cap. Their diameter, height, and periodicity are 240, 800, and 600 nm, respectively. The calculated new surface area is only three times larger than the original flat surface. Similarly, the microcolumns produced in SF_6 can be approximated as closely packed cones (Figure 1B). Their height and periodicity are 10.5 and 3 μm, respectively. Thus, compared to the original polished wafer, the surface area increases only by a factor of 6. As the LISMA produced in water is much more efficient in ion production than the structure formed in SF6, these estimates indicate that the ion production from these surfaces is not the result of their increased area.

(2) Surface Chemistry Due to Preparation Conditions. The three different preparation environments, air, SF_6, and water, result in chemically different surfaces. Although the true nature of these surfaces can only be determined by detailed analysis, one expects that air as a background gas results in a partially oxidized surface, whereas water promotes the formation of OH-terminated sites. In the presence of SF_6 during femtosecond laser processing, incorporation of both sulfur (~1000 ppm) and fluorine (~10 ppm) into the surface layer of LISMA was detected by secondary ion mass spectrometry.[39] Thus, the three processing environments leave the silicon surface in different chemical states. Further studies are required to understand the effect of the surface composition on the SLDI process.

(3) Thermal Confinement in LISMA. Formation of the microcolumns results in high aspect ratio submicrometer structures that exhibit the confinement of the energy deposited by the laser pulse. Dissipation of this energy through heat conduction is limited to the column axial direction, which results in the rapid rise of surface temperatures in these structures at relatively low fluences.[62]

In MALDI, primarily the matrix molecules absorb the laser energy. During laser irradiation and at the very early stage of plume expansion, the analyte molecules might experience a temperature higher than the sublimation temperature of the matrix molecules (ranging from 400 to 600 K),[54] but further plume expansion and collisions rapidly decrease the plume temperature.[46] The energy transfer between the matrix and analyte is also limited by an energy-transfer bottleneck.[55]

Silicon, however, has a melting point of over 1600 K and a sublimation temperature above 2800 K.[56] Although the temperature may not reach sublimation point, in SLDI on LISMA—as explained above—the surface temperature rises rapidly due to thermal confinement in the submicrometer structure. Furthermore, since it is a matrixless desorption method, the plume is less dense than in MALDI and the expansion cooling is negligible. At elevated laser fluence, the analyte molecules can acquire a significant amount of internal energy and undergo unimolecular decomposition.[57]

(4) Optical Properties of LISMA. Compared to bulk silicon, the altered chemical composition of the microcolumns results in enhanced optical absorption. The absorptance values are increased across the entire UV−visible spectrum, and significant absorption extends into the near-IR region, beyond the absorption edge defined by the band gap of bulk silicon.[39] Additional energy deposition is observed due to the presence of multiple scattering on the column arrays. Stronger optical absorption in combination with thermal confinement results in high surface temperatures at relatively low laser fluences.

(5) Reactions in Confined Plume. There are important consequences of the structured surface for the formation and dissipation of the plume. Compared to the original flat silicon surface, the troughs of the LISMA structure retain the laser plume at a higher density for a longer period of time. The bottom right panel of Figure 1C shows this scenario. As the columns heat up due to the laser radiation, the adjacent trough with submicrometer dimensions fills up with desorbed species. Assuming that the plume expands with ~300 m/s linear velocity, this takes ~1 ns. The dissipation of the plume from this confined volume takes place through the evacuation of the troughs. This process is limited by the reduced pumping speed within the LISMA structure. During the time the plume is retained, the in-plume reactions are enhanced. This effect is proportional to the plume density that, in turn, is a function of the laser fluence. As is shown in the next subsection, higher laser intensity can result in the buildup of significant alkali ion and electron density in the plume and, as a consequence, in the appearance of new ionic species in the spectrum.

(54) Vertes, A.; Irinyi, G.; Gijbels, R. *Anal. Chem.* **1993**, *65*, 2389−2393.

(55) Vertes, A.; Gijbels, R.; Levine, R. D. *Rapid Commun. Mass Spectrom.* **1990**, *4*, 228−233.

(56) http://webbook.nist.gov.

(57) Luo, G.; Marginean, I.; Vertes, A. *Anal. Chem.* **2002**, *74*, 6185−6190.

(58) Mao, S. S.; Mao, X.; Greif, R.; Russo, R. E. *Appl. Phys. Lett.* **1998**, *73*, 1331−1333.

(59) Afanasev, V. V.; Stesmans, A. *Europhys. Lett.* **2001**, *53*, 233−239.

(60) Zubarev, R. A.; Horn, D. M.; Fridriksson, E. K.; Kelleher, N. L.; Kruger, N. A.; Lewis, M. A.; Carpenter, B. K.; McLafferty, F. W. *Anal. Chem.* **2000**, *72*, 563−573.

(61) Leymarie, N.; Berg, E. A.; McComb, M. E.; O'Connor, P. B.; Grogan, J.; Oppenheim, F. G.; Costello, C. E. *Anal. Chem.* **2002**, *74*, 4124−4132.

(62) Sadeghi M.; Vertes A. *Appl. Surf. Sci.* **1998**, *127*−129, 226−234.

(6) Electron Emission and Fragmentation. In field-free MALDI experiments, electron emission from the stainless steel desorption substrate was observed.[50] Under the influence of nanosecond laser radiation, silicon surfaces are also known to emit electrons. At fluences below melting, Mao et al. demonstrated that the photoelectric effect induced electron emission for low fluences (30 mJ/cm^2), whereas thermionic emission of electrons dominated at higher fluences (80 mJ/cm^2).[58] Due to the modified surface composition of LISMA, these mechanisms can be significantly altered. There is, however, no information available on electron emission from the LISMA surfaces. In the following discussion, we assume that at least some electrons are emitted in delayed extraction experiments, where during the first ~100 ns after the laser pulse there is no external electric field. In continuous extraction experiments, the electron emission is suppressed by the reverse electric bias on the surface.

In the early phase of plume formation, these emitted electrons interact with the surface and mix with the plume of desorbed species including analytes, residual solvents, and products from other surface impurities (e.g., silanol groups). At low fluences, protons can originate from the electron-induced ionization[29] of these components either on the surface or in the plume,[15,18,51] and subsequent ion−molecule reactions can lead to protonated species. At increased laser power, the elevated electron density can neutralize the protons to form hydrogen-free radicals (H•).[59] Simultaneously, more alkali ions are released from the hot silicon surface that results in peptide−alkali adduct ion formation. In Figure 4C, panels f and e show the change of P14R molecular ions from protonated at low fluence (f) to sodiated at higher laser intensity (e).

The presence of H• in the plume can explain the onset of ISD and the formation of the fragmentation ladder observed in Figure 4A. Zubarev and co-workers demonstrated that in MALDI hydrogen atoms resulting from matrix photochemical reactions induced ISD.[53] The mechanism was deemed similar to the hydrogen atom attachment previously proposed to explain fragmentation in electron-capture dissociation (ECD) of multiply charged ions.[60] Even though there are no matrix molecules involved, in SLDI from LISMA hydrogen-free radicals can mediate ISD of singly charged peptide ions resulting in fragments similar to those in ECD.[60]

Equations 1 and 2 illustrate the fragmentation pathways that

(1)

(2)

(3)

P14R can follow after a hydrogen radical attack. The precursors are sodiated ions, and the charge can go to either fragment product. Equation 1 shows that, upon hydrogen atom attachment to the carbonyl group, the parent ion dissociates to form c and z•

fragments. Due to the cyclic structure of proline, N−C bond breakage is hindered.[61] The arginine is the only residue on the C-terminal that can break away as the free radical z fragment. This corresponds to the peak c$_{14}$, the only c type ion, in Figure 4A. Equation 2 shows that when the hydrogen atom attaches to the amine group the P14R dissociates into free radical, a$_n$•, and y segments. In eq 3, the a$_n$• continues the fast free radical fragmentation by sequentially losing carbonyl and 3,4-dihydro-2H-pyrrole, resulting in a series of a-type ions as is seen in the spectrum (Figure 4A).

Further proof of hydrogen atom attachment can be found in Figure 4C. Panels a−e show the isotope profiles of P14R fragment ions a$_{10}$, a$_{11}$, a$_{12}$, and c$_{14}$ and the [M + Na]$^+$ quasi-molecular ion at laser power 85, respectively. For reference, the isotope distribution of the protonated molecular ion, [M + H]$^+$, acquired at laser power 60 is displayed in panel f. The asterisk marks the monoisotopic peak in each profile. Compared to the profiles of c$_{14}$ and the molecular ions, the profiles of the a-type ions show a clear departure from their natural isotope distributions. In these spectra, the peak at two mass units above the monoisotopic species becomes the most abundant peak in the isotope profile. We attributed this to the appearance of [a$_n$ + 2H + Na]$^+$ ions (marked by the vertical arrows) formed by the attachment of two hydrogen radicals.

This process is described in eq 4, where some a-type radical

(4)

cations rearrange, break the cyclic structure, and react with two additional hydrogen atoms.

In this section, we demonstrated that at high laser power excess electrons contributed to hydrogen radical formation via proton/electron neutralization. These radicals promoted the ISD of peptides on the LISMA surface, giving structural information similar to ECD for de novo peptide sequencing.

CONCLUSIONS

Microcolumn arrays of laser-processed silicon were shown to be effective as SLDI substrates for the mass spectrometric analysis of peptides and synthetic polymers. The desorption/ionization threshold fluence and efficiency were strongly dependent on the surface morphology that was determined by the medium used in microstructuring. LISMA was capable of desorbing/ionizing peptides of up to 6000 Da molecular mass and exhibited low-femtomole detection limits. Depending on the laser power, LISMA behaved as a SLDI substrate for intact peptide analysis (low fluence) or produced structure-specific ions through ISD for top-down peptide sequencing (high fluence). The mechanism of ion formation under these conditions was attributed to the thermal, optical, and electron emission properties of the silicon microcolumns as well as to thermal and chemical confinement effects.

This new matrix-free SLDI substrate offers several advantages over existing systems. LISMA is more versatile than DIOS in the sense that varying the laser fluence enables interchanging between molecular ion detection and structure-specific fragmentation. It

is more robust than silicon nanowires as excessive laser exposure does not destroy the structure. In principle, the LISMA surface is reusable and can even be regenerated by further laser processing.

The analytical figures of merit for LISMA surfaces are less broadly tested than in the case of DIOS. We expect that the chemical modification of the microcolumn arrays, e.g., with silylation reagents, can not only change the surface chemical properties but also fine-tune the thermal and optical/electronic properties. How general the utility of ISD is for peptide sequencing remains to be seen. Although we have only tested bradykinin and the special case of P14R, we also showed that the mechanism of ISD on LISMA resembles that of ECD. In this mechanism, the hydrogen-free radicals attach to the amino and carbonyl groups and disrupt the peptide backbone while the labile posttranslational modifications are preserved. We expect that, similar to ECD, the cleavage sites should have little selectivity for particular amino acid residues. Further characterization of the broad ISD performance of LISMA is underway.

ACKNOWLEDGMENT